Modeling and Analysis of Grid-synchronizing Stability of a Type-IV Wind Turbine Under Grid Faults

Chen Zhang, Xu Cai, Marta Molinas, Atle Rygg

***Abstract*—Transient behavior and response of wind turbines have been extensively studied in the context of the low-voltage-ride-through (LVRT) for many years, in which the identified transients are mostly associated with circuit responses, whereas underlying stability issues relevant to converter control yet remain concealed. Recently, small-signal analyses of grid-tied converters have shown that the phase-locked-loop (PLL) may interact with other converter controls when synchronized to nonideal grids, if not properly treated, it may lead to oscillations. Enlightened by this, this paper will explore the PLL effects on the stability of a Type-IV wind turbine, however, from a large-signal analysis viewpoint. To achieve this, a nonlinear reduced-order model focusing on the transient interaction of PLL and the faulty grid is developed rigorously from the model assumption to verification. Based on this, the grid-synchronizing stability (GSS) provoked by grid faults is identified and the mechanism of which is revealed through the equal-area-principle (EAP). Then, impacts of system parameters (e.g. PLL bandwidth) on GSS margin are quantitatively evaluated by calculating the critical-clearing-time (CCT), and the acquired knowledge could be useful guidelines for PLL parameter design. Finally, all the analyses are verified by a switching model of the Type-IV wind turbine system in PSCAD/EMTDC.**

***Index Terms*—converter, synchronization, stability, PLL, grid faults, large-signal**

I. Introduction

Nowadays, voltage source converters (VSCs) are ubiquitous in power systems due to their wide applications in various types of renewable power generations [1]. For wind power conversion systems, usually, a back-to-back VSC is employed for conditioning and delivering the electric power from the wind generator to the AC grid, and in which a wind generator equipped with a full-scale VSC is typically referred to as the Type-IV wind turbine, whereas a doubly-fed induction generation in combination with a partial-scale VSC is known as the Type-III wind turbine.

Recently, field experiences in wind farms [3] and photovoltaic power plants [4] have shown that the VSCs are very susceptible to oscillate if connected to a weak AC grid. This issue immediately draws the attention and motivates the necessity of a comprehensive understanding and analysis of the stability issues specific to the VSC-based systems. In this respect, endeavors have been firstly made on the small-signal-stability (SSS) issue due to the consideration that those identified oscillations mostly occur when there is a moderate change of system configuration. Also, many analysis methods are available for this SSS issue,

among them, the impedance representation and the impedance-based frequency domain analysis of grid-tied VSCs is becoming popular since the impedance of a typical VSC can be easily derived either from analytical modeling or measurements (e.g. [5]-[8]). Moreover, the well-established frequency domain design and analysis tools (e.g. Nyquist criterion) can be easily modified and applied to the analysis of the grid-VSC system, e.g. the impedance-based stability criterion as presented in [9].

Although this paper will not focus on the SSS issue, one of the obtained knowledge could be of crucial importance and worth being noted is that the phase-locked-loop (PLL) can evidently interact with other converter controls under nonideal AC grids (e.g. [10] and [11]), if not properly treated, it may lead to oscillations. This also implies a necessity that the PLL should be properly modeled for such analyses.

Aside from the SSS, another aspect of the stability concern is the large-signal stability analysis, where nonlinear modeling of a dynamical system is required since the system states may no longer stay in the vicinity of equilibrium if the exogenous perturbation is large, this without no doubt makes the analysis tougher than the small-signal one. Large signal analysis of wind turbines can be traced back to the famous problem of low-voltage-ride-through (LVRT). And it is already known that the LVRT issue of the Type-III wind turbine is more challenging than that of the Type-IV since the generator of Type-III wind turbine is not physically isolated from the grid, thus grid disturbances will directly propagate to the rotor-side converter through the electromagnetic coupling of generator windings, typically resulting in large transients of rotor currents while the rotor-side converter has to be physically bypassed by a crowbar circuit for the purpose of protection. Due to this LVRT process, the rotor-side converter control will be inactive temporarily ([12]-[16]), due to which the control dynamics seem to play a less significant role than the circuit and winding dynamics under such an occasion. In contrast, Type-IV wind turbine could achieve uninterrupted control during LVRT owing to the electrical decoupling of the generator and the grid through the full-scale VSC (e.g. [17]-[19]), and they were noted for good LVRT capability [20] and usually regarded as controllable current sources for analysis. Despite this, large-signal analyses of both the Type-III and Type-IV wind turbine were yet focused on the transient responses of passive electromagnetic components and the grid was usually assumed as an ideal voltage excitation. Therefore, transient interactions between the grid and the converter controls were concealed. Until recently, enlightened by the SSS of VSCs, improper functioning of PLL under low-voltage conditions has been identified in e.g. [21] and [22]. It invokes the attention on the PLL nonlinearities and the grid effects in the large-signal analysis of wind turbines, where the stability issue may occur. This is particularly urgent for the Type-IV wind turbines, since their converter controls may consistently interact with a faulty grid during transients, from which the nonlinear dynamics of controls are provoked giving rise to the possibility of the large-signal stability issue.

In fact, some early works have implicitly noted the existence of large-signal stability issue of VSCs when the grid voltage suffered a severe sag. For example, prior works [23] and [24] adopted a simplified current phasor model for representing an aggregated wind farm. Then, the loss of equilibriums under depressed grid voltage is revealed and discussed, based on which,

some requirements on the limitation of active current injection during grid fault are recommended. In [25], the same conclusion is obtained from the improper functioning of PLL under grid voltage sags, where the positive feedback effect of PLL is identified. In essence, the analyses in [23]-[25] are equivalent and both are from static modeling and analysis viewpoint, whereas the stability related to the dynamical transition of system states were not covered. Latest works e.g. [26], [27] and [28] move further in this regard, by providing a dynamical analysis of PLL nonlinearity under grid fault conditions, from which the grid-synchronizing stability (GSS) issue is observed and the mechanism of which is preliminarily explained. Nevertheless, this subject is still less discussed, and more comprehensive analysis with respect to the quantitative analysis and evaluation of the stability margin is expected to be established. To this end and as an extension to the authors' previous work [26], this paper aims at a thorough analysis of the GSS issue of the Type-IV wind turbine, including the modeling, mechanism analysis, and stability assessment. The remaining content is briefly summarized as follows:

Section. II aims at developing a nonlinear model of the Type-IV wind turbine for GSS analysis. Section. III introduces the problem formulation, then followed by the mechanism analysis of GSS as well as a method for quantitatively evaluating the stability margin. Based on the method, section. IV provides a comprehensive numerical study of stability margin under various system configurations, from which a full picture of the GSS stability trend can be acquired. Section V verifies the GSS analysis through time domain simulations, where a switching model of a Type-IV wind turbine system is developed in PSCAD/EMTDC. Finally, section VI draws the main conclusions.

II. Nonlinear Modeling of the Type-IV Wind Turbine for Gird-synchronizing Stability Analysis

A. System description

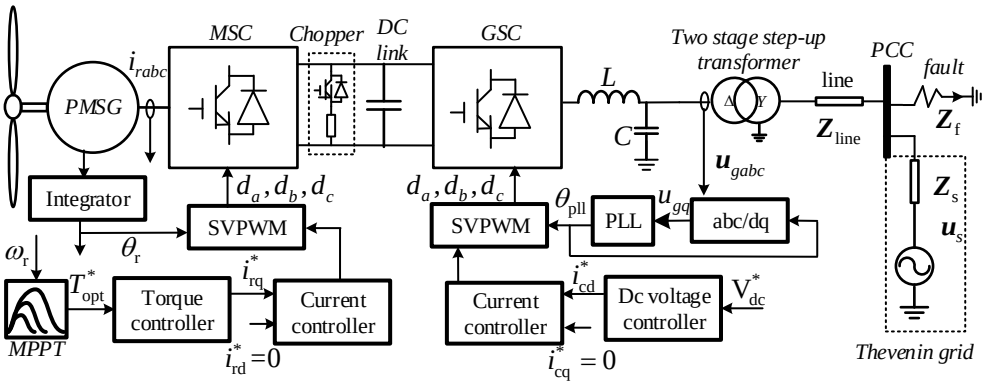

Fig. 1. A typical grid-tied Type-IV wind turbine system

Fig. 1 presents a typical Type-IV wind turbine system composed of a permanent magnet synchronous generator (PMSG), a back-to-back VSC, a two-stage step-up transformer for boosting the voltage to transmission level (e.g. from 0.69kV to 330 kV) and a Thevenin equivalent ac grid. Grid faults will be emulated by short circuits applied at the point of common coupling (PCC).

It is seen that there exists a relatively large impedance between the PCC and the terminal of the wind turbine, later analysis will show that this impedance is important for the GSS. Furthermore, the dc-side of the converter is equipped with a chopper circuit for preventing the dc voltage from overvoltage, which will typically be activated if the grid fault is severe.

The control system is generally composed of the machine side converter (MSC) control and grid side converter (GSC) control, one may refer to [2] for details. The inner current control loop (CCL) is usually tuned much faster than the outer loops (e.g. power and dc voltage control loop) for the purpose of dynamical decoupling. The tuning of PLL is usually aimed at achieving a fast settling time [1]. However, as mentioned before, recent SSS analysis already pointed out that a fast PLL that comparable to the CCL may have negative impacts on stability under nonideal AC grids (e.g. [5]-[11]). Therefore, from the grid-integration point of view, it is prone to tune the PLL to be slow. This work follows the same principle due to the stability is of major concern, where the PLL is much slower than the CCL.

B. Model assumptions for GSS analysis

For the mechanism analysis, a reduced-order model that focuses on the dynamics of concern is preferred since it can provide more insights into properties. Fortunately, many dynamical systems exhibit a multi-timescale characteristic, which allows us to formulate reduced-order models for the problems of different time scales. In this study, a nonlinear model will be proposed based on the following considerations relevant to GSS analysis. The first consideration that under grid faults the action of dc chopper protection [20] is almost inevitable due to the power imbalance between the MSC and GSC. Once the dc chopper is activated, the consequences are:

1) The dc voltage can be assumed steady due to the protection of dc chopper.

2) The dc voltage controller will wind up and its output (i.e. current reference) is saturated at: $I_{\mathrm{d}}^{\mathrm{ref}} \approx I_{\mathrm{d}}^{\mathrm{sat}}$.

3) The MSC can be omitted due to the isolating effect after the dc chopper is inserted.

Based on the above consequences, the first model assumption (i.e. MA1) is summarized as that the dc voltage of the converter is assumed steady during grid faults (denoted by MA1), as a result, the overall system can be simplified to a grid-side converter with a constant dc voltage as shown in Fig. 2 (a).

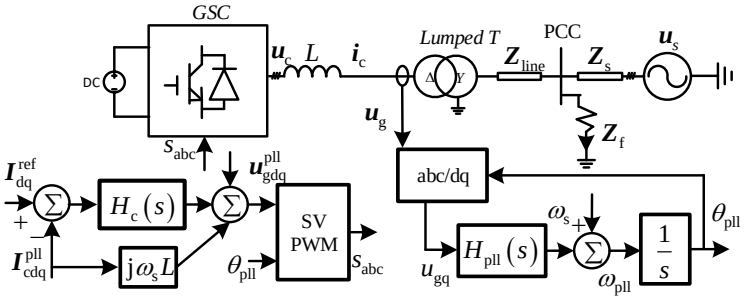

(a) Reduced system configuration based on MA1

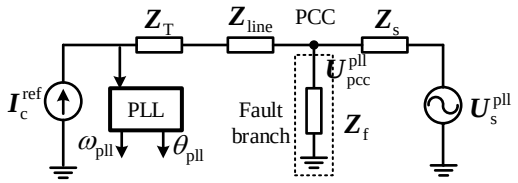

(b) A circuit representation of the model (a) further considering MA2

Fig. 2 Model reduction of a grid-synchronized Type-IV wind turbine system

Table I Brief list of model assumptions for GSS modeling

Model assumption	Consequence
MA1: a constant dc voltage	1) A stable dc voltage; 2) Constant current reference; 3) MSC can be omitted.
MA2: CCL is much faster than PLL	CCL is quasi-static in PLL time scale.

Another assumption is directly obtained from the afore-mentioned analysis that the PLL is much slower than the CCL (i.e. model assumption2, MA2) so that the SSS issue caused by the interaction of PLL and CCL can be avoided for the large-signal analysis. As a result, dynamics of the CCL, if viewed from the PLL time scale, can be assumed in the quasi-static state, i.e. $\boldsymbol{I}_c^{ref} \approx \boldsymbol{I}_c^{pll}$ (a brief justification is given in Appendix. A based on the singular perturbation analysis). A summary of these two assumptions for GSS modeling is listed in Table I.

Combining MA1 and MA2, a circuit description of the reduced system is presented in Fig. 2 (b), from which it is seen that the PLL-related dynamics are reserved whereas other control dynamics are reduced. Validation of the model assumptions will be presented in section V. (Note that, the superscript "pll" denotes variables in PLL rotating frame. For convenient analysis, all the system variables are projected on the PLL reference frame, which means e.g. $\boldsymbol{Z}_T\left(\mathrm{j}\omega_{pll}\right)$ and $\boldsymbol{U}_s^{pll} = U_s\, \mathrm{e}^{\mathrm{j}\left(\theta_s - \theta_{pll}\right)}$ are all PLL-dependent variables).

C. Nonlinear analytical modeling of the reduced system for GSS analysis

According to the circuit model in Fig. 2 (b), the input of PLL can be written as:

$$u_q^{pll} = \mathrm{Im}\left\{\boldsymbol{I}_c^{ref}\boldsymbol{Z}_\Sigma\left(\omega_{pll}\right) + \boldsymbol{U}_{pcc}^{pll}\right\} \quad (1)$$

where $\boldsymbol{Z}_\Sigma\left(\omega_{pll}\right) = \boldsymbol{Z}_T\left(\omega_{pll}\right) + \boldsymbol{Z}_{line}\left(\omega_{pll}\right)$ is the aggregated impedance of the transformer and the transmission line. $\boldsymbol{Z}_\Sigma\left(\omega_{pll}\right) = R_\Sigma + \mathrm{j}\omega_{pll}L_\Sigma$. $\boldsymbol{I}_c^{ref} = I_{cd}^{ref} + \mathrm{j}I_{cq}^{ref}$, $\boldsymbol{U}_{pcc}^{pll} = \left|\boldsymbol{U}_{pcc}^{pll}\right|\exp\left(-\mathrm{j}\delta_{pll}\right)$, $\delta_{pll} = \theta_{pll} - \theta_{pcc}$ is the angle difference between the PLL rotating frame and the PCC voltage vector.

According to the control blocks of PLL in Fig. 2 (a)

$$\theta_{\mathrm{pll}}=\int\left(k_{\mathrm{p}}u_{\mathrm{q}}^{\mathrm{pll}}+k_i\int u_{\mathrm{q}}^{\mathrm{pll}}dt\right)dt+\int \omega_s dt \quad (2)$$

is obtained, and substituting $u_{\mathrm{q}}^{\mathrm{pll}}$ into (2) the following second-order system (in per unit format) can be obtained:

$$\begin{cases}\underbrace{\left(\dfrac{\omega_{\mathrm{b}}-k_{\mathrm{p}}\bar{I}_{\mathrm{cd}}^{\mathrm{ref}}\bar{X}_{\Sigma}}{k_{\mathrm{i}}}\right)}_{T_{\mathrm{pll}}}\cdot\dfrac{d\Delta\bar{\omega}_{\mathrm{pll}}}{dt}=\underbrace{\bar{I}_{\mathrm{cq}}^{\mathrm{ref}}\bar{R}_{\Sigma}+\bar{I}_{\mathrm{cd}}^{\mathrm{ref}}\bar{\mathrm{X}}_{\Sigma}}_{f}-\underbrace{\left|\bar{\boldsymbol{U}}_{\mathrm{pcc}}\right|\sin\left(\delta_{\mathrm{pll}}\right)}_{g}-\underbrace{\left(\omega_{\mathrm{b}}\left|\bar{\boldsymbol{U}}_{\mathrm{pcc}}\right|\cos\delta_{\mathrm{pll0}}\dfrac{k_{\mathrm{p}}}{k_{\mathrm{i}}}-\bar{I}_{\mathrm{cd}}^{\mathrm{ref}}\bar{X}_{\Sigma}\right)}_{D_{\mathrm{pll}}}\cdot\Delta\bar{\omega}_{\mathrm{pll}} \\ \dfrac{d\delta_{\mathrm{pll}}}{dt}=\omega_{\mathrm{b}}\cdot\Delta\bar{\omega}_{\mathrm{pll}}\end{cases} \quad (3)$$

where $\omega_{\mathrm{b}}=2\pi\cdot 50 rad/s$ is the base angular speed, and $\Delta\bar{\omega}_{\mathrm{pll}}=\left(\bar{\omega}_{\mathrm{pll}}-\bar{\omega}_{\mathrm{s}}\right)$.

Table II Model comparison of the proposed model and a SG

Nonlinear model of GSS analysis, i.e. (3)	Classic second-order model of a SG [29]
Input: $f=\bar{I}_{\mathrm{cq}}^{\mathrm{ref}}\bar{R}_{\Sigma}+\bar{I}_{\mathrm{cd}}^{\mathrm{ref}}\bar{\mathrm{X}}_{\Sigma}$	Mechanical torque: $T_{\mathrm{m}}=\mathrm{const}$
Input: $g=\left\|\bar{\boldsymbol{U}}_{\mathrm{pcc}}^{\mathrm{pll}}\right\|\sin\left(\delta_{\mathrm{pll}}\right)$	Electromagnetic torque: $T_{\mathrm{e}}=\dfrac{U_sU_g}{X_s}\sin\delta_g$.
Parameter: $T_{\mathrm{pll}}=\left(\omega_{\mathrm{b}}-k_{\mathrm{p}}\bar{I}_{\mathrm{cd}}^{\mathrm{ref}}\bar{X}_{\Sigma}\right)/k_{\mathrm{i}}$	Inertial constant: $H_{\mathrm{s}}=\dfrac{0.5J\omega_s^2}{S_n}=\mathrm{const}$
Parameter: $D_{\mathrm{pll}}=\left(\omega_{\mathrm{b}}\left\|\bar{\boldsymbol{U}}_{\mathrm{pcc}}^{\mathrm{pll}}\right\|\cos\delta_{\mathrm{pll0}}\cdot k_{\mathrm{p}}\right)/k_{\mathrm{i}}-\bar{I}_{\mathrm{cd}}^{\mathrm{ref}}\bar{X}_{\Sigma}$	Damping: $D_{\mathrm{s}}=\mathrm{const}$

From (3) it is seen that the nonlinear model for GSS analysis resembles the classical motion equation of an SG [29]. A comparison is shown in Table II, where the inputs f and g resemble the mechanical and electromagnetic torque respectively, whereas the T_{pll} and D_{pll} resemble the inertia and damping of the SG. It is worth mentioning again that, prior works e.g. [23]-[25], in fact, only take the static characteristics of f and g into account, where the positive feedback effect of PLL in [25] can be explained here as: $|f|\geq|g|, g\to 0$ under low-voltage conditions. Moreover, since f is proportional to the line impedance, thus a stronger positive feedback effect is expected if the grid fault is far away from the terminal of the wind turbine.

III. Problem Formulation and Analysis of Grid-synchronizing Stability

A. Problem formulation of the GSS

Since (3) is similar to the SG motion equation, it is expected that the Type-IV wind turbine will behave similarly as the SG under grid faults. For the SG, this problem is referred to as the *transient rotor angle stability*, however, for VSCs, there does not exist a similarly physical quantity, thus this problem is interpreted as the grid-synchronizing stability (GSS) since the main objective is to remain synchronization after the grid fault is cleared.

On the other hand, the Equal Area Principle (EAP) [29] for the transient stability analysis of the SG can be applied to this GSS analysis due to the similarity in models. It should be noted that, as the time constant in (3) (dependent on the value of PLL bandwidth) is usually much smaller than the physical inertia of the SG, dynamics of (3) is more sensitive to the characteristic of the grid fault, e.g. the magnitude and phase of *g*, thus both of this two factors will be considered in the later mechanism analysis.

B. Mechanism analysis of the GSS

In general, based on the knowledge of transient rotor angle stability of the SG, the GSS of a Type-IV wind turbine can be interpreted as that if (3) has an equilibrium that is locally stable and deviation of states during the grid fault period is bounded in a region predicted by the EAP, then the system will be stable.

This can be qualitatively illustrated in Fig. 3, where both a severe and less severe grid fault condition is considered. It should be noted that the input f in (3) is irrelevant with grid faults according to the consequence of MA1, hence f remains steady at the pre- and post-fault states (i.e. $f^{0-} = f^{0+}$). In contrast, the input g of (3) is dependent on the PCC voltage, i.e. grid fault, hence its characteristic will vary drastically if the grid fault is severe (e.g. g^{0-} and g^{0+} in Fig. 3(a)).

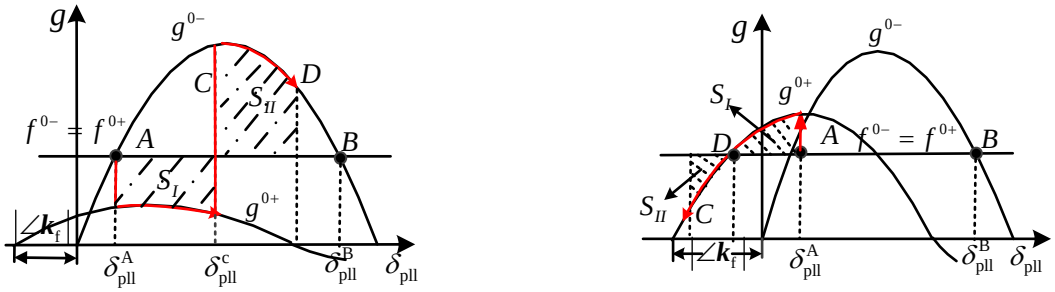

(a) Nonexistence of new equilibrium (a severe grid fault) (b) Existence of new equilibrium (a less severe grid fault)

Fig. 3. Mechanism Analysis of the GSS based on EAP (The superscript "0+" denotes post-fault instant, whereas "0-" denotes pre-fault instant.)

Regarding the sever grid fault case in Fig. 3(a), it is identified that there does not exist a new equilibrium point in the fault duration since there are no intersections between g^{0+} and f. Hence the point A is the only physically existent equilibrium and stability of this point can be assured only if the grid fault is cleared fast enough, the criterion of which can be formally stated by the EAP i.e. $\exists S_{II}\left(\Delta\omega_{\text{pll}} = 0, \delta_{\text{pll}} \le \delta_{\text{pll}}^{B}\right): S_I = S_{II}$ is met. Intuitively, if the grid fault is cleared too late, e.g. at an instant where $\delta_{\text{pll}}^{\text{c}}$ is close to δ_{pll}^{B}, then the deceleration area S_{II} will not adequate for compensating the acceleration area S_I, indicating a loss of synchronization. As for the case of a less severe grid fault in Fig. 3 (b), a new equilibrium (point D) is existent in the fault duration, which means the system can be stabilized to that point during the grid fault if the EAP is met. This implies that the system is of less possibility to the loss of synchronization under a small voltage sag.

One may also observe that the post-fault characteristics of both cases could incorporate some phase shifts due to the types of grid faults. This phase shift can lead to the change of the area S_I, however, effects of phase shifts could be marginal if the grid voltage is already very small (i.e. under a severe grid fault), it will be discussed in section IV.

C. A Method for quantitative analysis of the GSS margin

Due to the above consideration, GSS analysis will focus on the severe grid fault conditions. From the mechanism analysis of Fig. 3 (a) it is obtained that, if the grid fault is cleared at an angle $\delta_{\text{pll}}^{\text{c}}$ where the critical condition of EAP is met (i.e. $\exists \delta_{\text{pll}}^{\text{CCA}} : S_I = S_{II}^{\max}$), then this angle ($\delta_{\text{pll}}^{\text{CCA}}$) is referred to as the Critical Clearing Angle (CCA). Clearly, the CCA can be a metric of the GSS margin since a large value of $\delta_{\text{pll}}^{\text{CCA}}$ indicates more margin. Next, to allow a quantitative evaluation of the CCA, the post-fault characteristic g^{0+} (i.e. $g^{0+} = \text{Im}\left\{\boldsymbol{U}_{\text{pcc}}^{0+}\right\}$) should be further determined, which is basically fulfilled by a circuit analysis as follows.

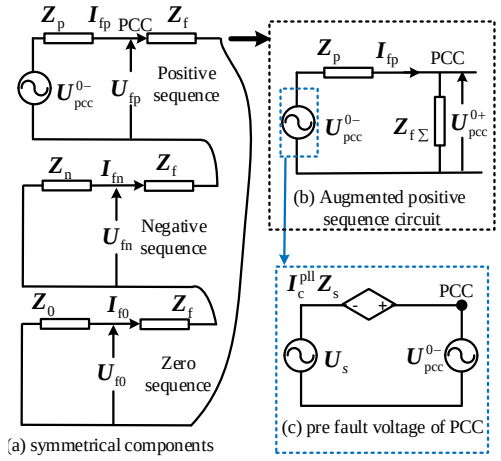

Fig. 4 Circuit analysis of grid faults based on symmetrical components

Considering a general case in which the grid fault could be unbalanced, e.g. a phase A fault with a short circuit impedance $\boldsymbol{Z}_{\text{f}}$ is applied at PCC. Then, the short circuit branch (i.e. faulty branch) can be characterized as:

$$\begin{cases} \boldsymbol{I}_{\text{fb}} = \boldsymbol{I}_{\text{fc}} = 0 \\ \boldsymbol{U}_{\text{fa}} = \boldsymbol{I}_{\text{fa}} \boldsymbol{Z}_{\text{f}} \end{cases} \rightarrow \begin{cases} \boldsymbol{I}_{\text{fp}} = \boldsymbol{I}_{\text{fn}} = \boldsymbol{I}_{\text{f0}} \\ \left(\boldsymbol{U}_{\text{fp}} - \boldsymbol{I}_{\text{fp}} \boldsymbol{Z}_{\text{f}}\right) + \left(\boldsymbol{U}_{\text{fn}} - \boldsymbol{I}_{\text{fn}} \boldsymbol{Z}_{\text{f}}\right) + \left(\boldsymbol{U}_{\text{f0}} - \boldsymbol{I}_{\text{f0}} \boldsymbol{Z}_{\text{f}}\right) = 0 \end{cases} \tag{4}$$

where, $\boldsymbol{I}_{\text{fa}}, \boldsymbol{I}_{\text{fb}}, \boldsymbol{I}_{\text{fc}}$ are the currents flow into the fault branch, and $\boldsymbol{I}_{\text{fp}}, \boldsymbol{I}_{\text{fn}}, \boldsymbol{I}_{\text{f0}}$ are the symmetrical components. Based on the equations, the original three-phase circuit (see Fig. 2 (b)) can be decomposed into symmetrical components, see Fig. 4 (a). Then, the augmented positive sequence circuit can be obtained in Fig. 4 (b), where the pre-fault PCC voltage in Fig. 4 (c) is written as

$$\bar{\boldsymbol{U}}_{\mathrm{pcc}}^{0-}=\bar{\boldsymbol{I}}_{\mathrm{c}}^{\mathrm{pll}}\bar{\boldsymbol{Z}}_{\mathrm{s}}+\bar{\boldsymbol{U}}_{\mathrm{s}} \quad (5)$$

Generally, various types of grid faults can be emulated by modifying the value of $\boldsymbol{Z}_{\mathrm{f}\Sigma}$ in the augmented positive sequence circuit. In this work, the balanced grid fault is considered since it is known as the *worst* case. Hence, the augmented impedance is reduced to: $\bar{\boldsymbol{Z}}_{\mathrm{f}\Sigma}=\bar{\boldsymbol{Z}}_{\mathrm{f}}$, whereas the positive sequence impedance of the grid is: $\bar{\boldsymbol{Z}}_{\mathrm{p}}=\bar{\boldsymbol{Z}}_{\mathrm{s}}$.

As a result, the post-fault PCC voltage is written as

$$\bar{\boldsymbol{U}}_{\mathrm{pcc}}^{0+}=\frac{\bar{\boldsymbol{Z}}_{\mathrm{f}}}{\bar{\boldsymbol{Z}}_{\mathrm{s}}+\bar{\boldsymbol{Z}}_{\mathrm{f}}}\bar{\boldsymbol{U}}_{\mathrm{pcc}}^{0-}=\boldsymbol{k}_{\mathrm{f}}\bar{\boldsymbol{U}}_{\mathrm{pcc}}^{0-} \quad (6)$$

according to Fig. 4 (b). Finally, the model of the post-fault g^{0+} is obtained:

$$g^{0+}=\mathrm{Im}\left\{\bar{\boldsymbol{U}}_{\mathrm{pcc}}^{0+}\right\}=\left|\boldsymbol{k}_{\mathrm{f}}\right|\left|\bar{\boldsymbol{U}}_{\mathrm{pcc}}^{0-}\right|\sin\left(\delta_{\mathrm{pll}}-\angle\boldsymbol{k}_{\mathrm{f}}\right) \quad (7)$$

where $\boldsymbol{k}_{\mathrm{f}}$ is complex-valued coefficient related with $\bar{\boldsymbol{Z}}_{\mathrm{f}}$. (7) can be viewed as a curve deformation (shift and compress) of the pre-fault characteristic, i.e. $g^{0-}=\mathrm{Im}\left\{\bar{\boldsymbol{U}}_{\mathrm{pcc}}^{0-}\right\}=\left|\bar{\boldsymbol{U}}_{\mathrm{pcc}}^{0-}\right|\sin\left(\delta_{\mathrm{pll}}\right)$, based on this model the shapes of g^{0+} in Fig. 3 is well-explained.

Further, according to the EAP and Fig. 3 (a), the critical condition $\exists\delta_{\mathrm{pll}}^{\mathrm{CCA}}: S_I=S_{II}^{\max}$ is explicitly written as:

$$\underbrace{\int_{\delta_{\mathrm{pll}}^{\mathrm{A}}}^{\delta_{\mathrm{pll}}^{\mathrm{CCA}}}\left(f_{\mathrm{m}}^{0-}-g^{0-}\right)\cdot d\delta_{\mathrm{pll}}}_{S_I}=\underbrace{-\int_{\delta_{\mathrm{pll}}^{\mathrm{CCA}}}^{\delta_{\mathrm{pll}}^{\mathrm{B}}}\left(f_{\mathrm{m}}^{0+}-g^{0+}\right)\cdot d\delta_{\mathrm{pll}}}_{S_{II}^{\max}} \quad (8)$$

Since all the functions in (8) are known according to (3) and (7), $\delta_{\mathrm{pll}}^{\mathrm{CCA}}$ can be numerically calculated by solving the nonlinear algebraic equation (8). Considering that $\delta_{\mathrm{pll}}^{\mathrm{CCA}}$ is not a physical rotor angle and is not intuitive for this analysis, instead, the Critical Clearing Time (CCT) denoting the longest fault duration allowable while remaining stable can be adopted. The CCT can be estimated by substituting the numerical solution of $\delta_{\mathrm{pll}}^{\mathrm{CCA}}$ into the angular motion equation in (3), yields

$$t_{\mathrm{cct}}=\frac{\left(\delta_{\mathrm{pll}}^{\mathrm{CCA}}-\delta_{\mathrm{pll}}^{A}\right)}{k_{\mathrm{c}}\omega_{\mathrm{b}}\cdot\Delta\bar{\omega}_{\mathrm{pll}}^{\mathrm{cct}}}=\frac{\left(\delta_{\mathrm{pll}}^{\mathrm{CCA}}-\delta_{\mathrm{pll}}^{A}\right)}{k_{\mathrm{c}}}\sqrt{\frac{T_{\mathrm{pll}}}{2S_I\omega_{\mathrm{b}}}} \quad (9)$$

where $\Delta\bar{\omega}_{\mathrm{pll}}^{\mathrm{cct}}=\sqrt{\frac{2S_{\mathrm{I}}}{T_{\mathrm{pll}}\omega_{\mathrm{b}}}}$. It is noted that in order to achieve an analytical equation as (9), an approximation is made on the integral of the motion equation of (3), i.e. $\int_0^{t_{\mathrm{cct}}}\omega_{\mathrm{b}}\cdot\Delta\bar{\omega}_{\mathrm{pll}}\cdot dt$ is approximated by the area $\left(t_{\mathrm{cct}}\omega_{\mathrm{b}}\cdot\Delta\bar{\omega}_{\mathrm{pll}}^{\mathrm{cct}}\right)\cdot k_{\mathrm{c}}$, where $k_{\mathrm{c}}\le 1$. If a linear increase of $\Delta\bar{\omega}_{\mathrm{pll}}$ during grid faults is assumed, then $k_{\mathrm{c}}=1/2$ is obtained, in fact, usually $\Delta\bar{\omega}_{\mathrm{pll}}$ does not increase linearly due to the nonlinear characteristic of g^{0+}, thus a value around but not specific to $k_{\mathrm{c}}=1/2$ can be selected for a better approximant. This will be discussed in section IV.C.

IV. A Numerical Study of Grid-synchronizing Stability Margin

Based on the introduced method, in this section, the GSS margin will be evaluated under various system configurations to acquire a full picture of the stability trend.

A. Impact of PLL bandwidth on the CCT

First, a qualitative observation is that the time constant T_{pll} is proportional to the CCT according to (9). This resembles the inertial effects of an SG, however, T_{pll} is not physically dependent on the rotating mass but on the parameters of PLL (see the model in Table II). Hence, a large PLL bandwidth is equivalent to a small time constant T_{pll}, thus a small CCT and stability margin.

Then, a numerical analysis of PLL bandwidth against the CCT is conducted and plotted in Fig. 5 (a). It is seen that the CCTs are drastically increased (i.e. the GSS margin is increased) as the PLL bandwidth reduces. Besides, the depth of PCC voltage drops can also affect the CC, for a less severe grid fault (i.e. a larger magnitude of g^{0+}), the overall CCT curves are lifted up indicating an improvement on GSS margin. However, this improvement is limited if compared to the effects of PLL.

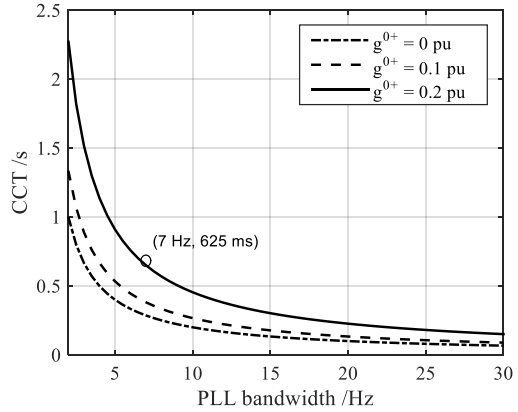

(a) Impacts of PLL bandwidth on CCT ($\bar{\boldsymbol{I}}_{\text{c}} = 1 + 0 \cdot \text{j}$, $\bar{\boldsymbol{Z}}_{\Sigma} = 0.2\text{j}$, $\bar{\boldsymbol{Z}}_{\text{s}} = 0.1\text{j}$)

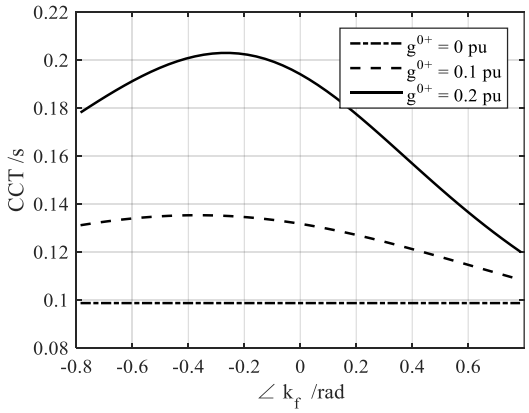

(b) Impacts of voltage sags and phase shifts on CCT ($\bar{\boldsymbol{I}}_{\text{c}} = 1 + 0 \cdot \text{j}$, $\bar{\boldsymbol{Z}}_{\Sigma} = 0.2\text{j}$, $\bar{\boldsymbol{Z}}_{\text{s}} = 0.1\text{j}$, PLL = 20 Hz)

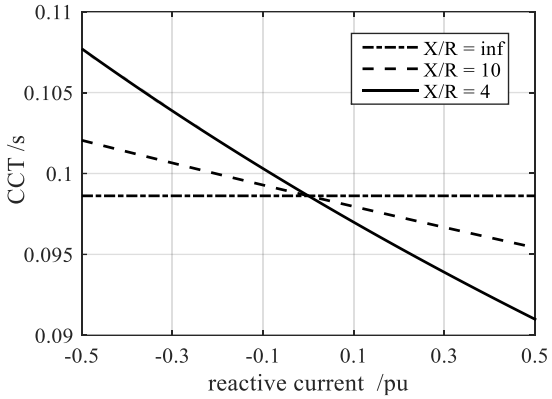

(c) Impacts of reactive current injection on CCT ($\bar{I}_{cd}=1$, $\bar{X}_{\Sigma}=0.2\mathrm{j}$, $\bar{R}_{\Sigma}$ is given by the X/R ratio, $\bar{\boldsymbol{Z}}_{s}=0.1\mathrm{j}$, PLL = 20 Hz, g^{0+}=0)

Fig. 5. Impacts of system parameters on GSS margin

B. Impact of voltage sags and phase shifts on CCT

According to (7), different levels of PCC voltage sags and phase shifts can be emulated by modifying the short circuit impedance $\boldsymbol{Z}_{\mathrm{f}}$. As shown in Fig. 5 (b), the phase shift varies between this range $\left[-\frac{\pi}{4},\frac{\pi}{4}\right]$, for a small negative phase shift, the CCT is increased since the acceleration area S_{I} is reduced as implied in Fig. 3 (a). However, if the negative phase shift is large, the CCT may be reduced due to the nonlinear characteristics of g^{0+}. This can also be explained by Fig. 3 (a), where the negative part of g^{0+} can take effects on the acceleration area S_{I} if the phase shift to the left is large. In general, the effects of phase shifts on CCT are marginal, particularly under a severe grid fault where the magnitude of the grid voltage is small.

On the other hand, under a less severe grid fault, an interesting effect of the phase shift is that it determines the initial direction of the frequency swing and motion. As illustrated in Fig. 3 (b), where the initial direction of frequency motion is negative (i.e. deceleration) since this condition $g^{0+}>f^{0+}$ is met at the fault instant. By contrast, imagine that if there are no phase shifts presented in g^{0+}, then at the fault instant this condition $g^{0+}<f^{0+}$ will be met, indicating the initial direction of frequency motion is positive, i.e. acceleration. This will be explained later by the measured phase portraits in simulation analysis.

C. Impact of reactive current injections on CCT

At last, the impacts of reactive current injections on the CCT are presented in Fig. 5 (c). Based on $f=\bar{I}_{\mathrm{cd}}^{\mathrm{ref}}\bar{X}_{\Sigma}+\bar{I}_{\mathrm{cq}}^{\mathrm{ref}}\bar{R}_{\Sigma}$, it is noticed that the reactive current injection only takes effects on the GSS if the line impedance has a resistive part, otherwise, the CCT is not affected by the reactive current injections as justified by the plots with a condition $X/R\to\inf$. If the line resistance exists, then the reactive current injection will take effects on CCT. By comparing the plots under *X/R* = 4 and X/R = 10 it is seen that the larger the line resistance, the greater the effects. Besides, a negative reactive current injection (i.e. inductive current since the positive direction is flowing into the grid) is beneficial for GSS. Also, it is noted that, if the controls are designed to drive

$f = 0$, i.e. $\bar{I}_{cd}^{ref}\bar{X}_{\Sigma}+\bar{I}_{cq}^{ref}\bar{R}_{\Sigma} = 0$, then the control law in [28] is obtained. In this way, the wind turbine can be stabilized at the origin during the grid fault.

V. Time Domain Verifications and Analysis of GSS

This section aims to validate the proposed nonlinear model and associated GSS analysis. Simulation is conducted in PSCAD/EMTDC, where a switching model of the Type-IV wind turbine system is developed. Main parameters of the simulation system are listed in Table III.

Table III Main parameters of the simulation system

PMSG		Wind rotor	
Variables	Values	Controller	Values
Frequency	13 Hz	Power rating	2 MW
Voltage	690 V	Rotor diameter	80 m
Pole pairs	32	Air density	1.225 kg/m^3
Magnetic flux	7.57 Wb	Rated speed	2.253 rad/s
Stator resistance	0.00082 ohm	Inertia	3.5 s
D axis reactance	1.5 mH	Tip ratio	7.8
Q axis reactance	1.5 mH	C_p	0.417
Inertia time constant	0.5 s		
VSC and control parameters			
Variables	Values	Controller	Values
Power rating	2 MVA	DCL	k_p= 0.4, k_i = 8
Rate voltage	0.69 kV (RMS)	TCL	k_p= 0.1, k_i = 20
DC voltage	1.1 kV	CCL of GSC	k_p= 0.06, k_i = 6
DC capacitance	10 mF	CCL of MSC	k_p= 0.6, k_i = 126
Switching frequency	2.4 kHz	PLL	variable

A. Verification of the model assumptions

When deriving the nonlinear model for GSS analysis, two assumptions are made with respect to the dc voltage and current control (see Table I for the summary), in what follows, they will be verified under a balanced and unbalanced grid fault condition, and for each condition, transient responses under two sets of PLL bandwidths are compared.

In the first place, a balanced grid fault case is shown in Fig. 6 (a), the voltage sag at PCC is manipulated by the short circuit impedance $\boldsymbol{Z}_f$ to achieve the condition: $\left|f^{0+}\right| = 0.2 < \left|g^{0+}\right| = 0.3\,pu$ As a result, the system is stable according to the mechanism analysis in Fig. 3 (b). Under this configuration, it can be observed from the dc voltage transient waveform (see E_{dc}) that, it remains steady in the fault period due to the fast activation of dc chopper protection. Further, since the isolation effect of the dc chopper,

MSC dynamics are almost unaffected by grid disturbances (see the plots of ω_g, T_{eg}). These observations prove that MA1 is valid. Next, by comparing the PLL (ω_{pll}) and the active current (I_{cd}) waveforms it can be obtained that, despite the variation of PLL frequency, the active current can remain controlled and steady in the fault duration, which means the quasi-static model of current in PLL time frame (i.e. MA2) is also feasible. In addition, by comparing the transient responses under two sets of PLL bandwidths it is seen that the major difference is on the ω_{pll}, where the frequency deviation is small if a small PLL bandwidth is employed.

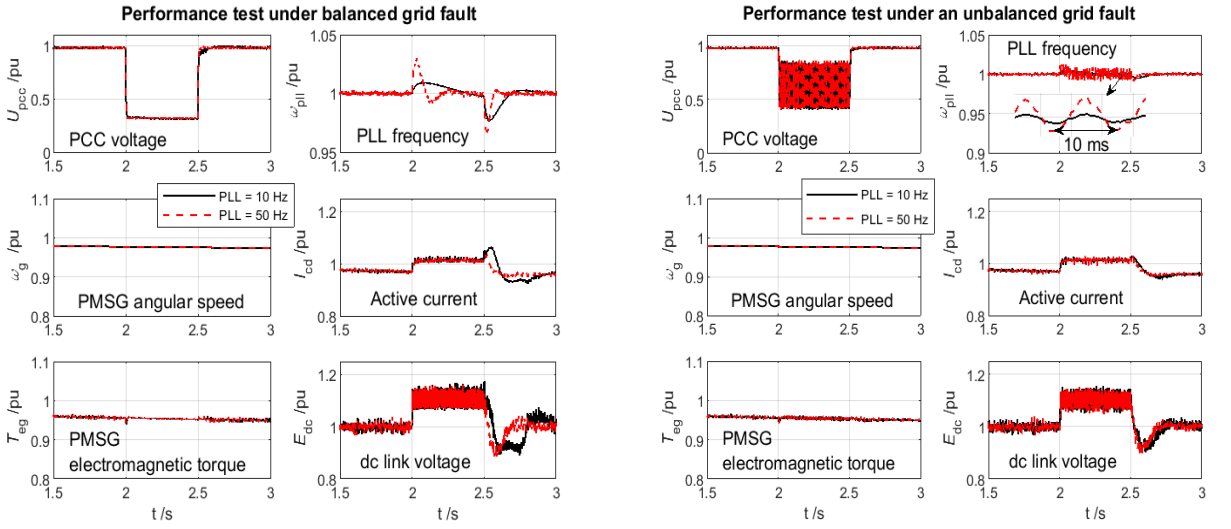

(a) Transient responses under a balanced grid fault

(b) Transient responses under an unbalanced grid fault (phase A)

Fig. 6. Simulation analysis of model assumptions (grid fault is applied at 2s with a duration of 500 ms, $\bar{\boldsymbol{I}}_c \approx 1+0\cdot \mathrm{j}$, $\bar{\boldsymbol{Z}}_{\Sigma} = 0.2\mathrm{j}$, $\bar{\boldsymbol{Z}}_s = 0.1\mathrm{j}$ pu)

Since the derivation of the post-fault PCC voltage (i.e. g^{0+}) is generalized for unbalanced cases in section III.C, it is worth to verify the model under unbalanced grid faults even though the GSS is focused on balanced cases (i.e. the worst case). In this regard, simulations under an unbalanced grid fault are presented in Fig. 6 (b). From which it is seen that the model assumptions (i.e. MA1 and MA2) are still valid since both the dc voltage and current remain steady in the fault period. It is also noted that the unbalanced grid fault leads to the oscillation of ω_{pll} at double-line frequency. However, the impacts of this variation on grid synchronization are negligible, since its mean value over-half-line period is approximately zero. In addition, the deviation of frequency and the amplitude of oscillation is still smaller under a small PLL bandwidth.

Therefore, it can be concluded that the model assumptions are valid. In what follows, the effectiveness of the mechanism analysis will be further verified.

B. Verification of the mechanism analysis of GSS

To achieve a better illustration and verification of the GSS mechanisms, measured phase portraits of states $\left(\delta_{pll}, \Delta\omega_{pll}\right)$ will be plotted. In Fig. 7 (a), the phase portrait under a less severe grid fault (i.e. $\boldsymbol{k}_f$ = 0.5 by manipulating short circuit impedance $\mathbf{Z}_f$) is

presented. According to the simulation configurations, since the condition $\left|g^{0+}\right| \approx 0.5 > \left|f^{0+}\right| = \left|\mathrm{Im}\left\{\bar{\boldsymbol{Z}}_{\Sigma}\bar{\boldsymbol{I}}_{\mathrm{c}}\right\}\right| = 0.2$ is satisfied, the system should have a new equilibrium in the fault period. Thus, the trajectories of the phase portrait should follow the mechanism depicted in Fig. 3 (b). It can be clearly confirmed as follows that the phase portrait is well supported by the mechanism analysis. Specifically the Trace I in Fig. 7 (a) corresponds to the state transition from point A to point C (new equilibrium) in Fig. 3 (b), whereas the Trace II corresponds to the state transition from point C and back to point A.

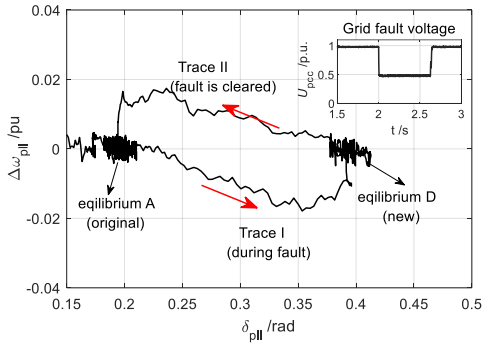

(a) Phase portrait under a less severe grid fault ($\left|\boldsymbol{k}_f\right| = 0.5$)

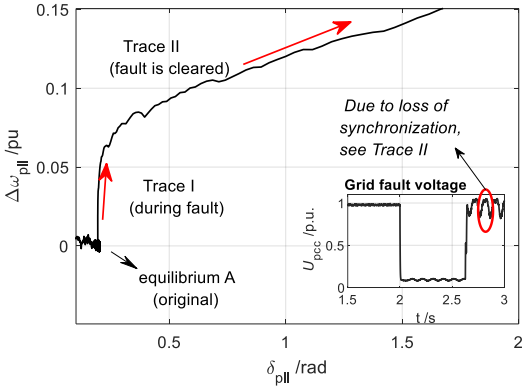

(b) Phase portrait under a severe grid fault ($\left|\boldsymbol{k}_f\right| = 0.1$)

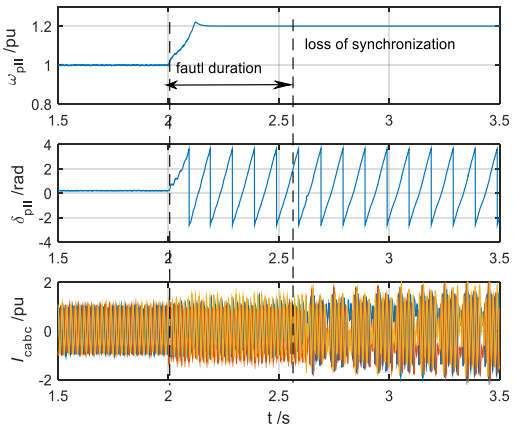

(c) Time domain waveforms of the sever grid fault case ($\left|\boldsymbol{k}_f\right| = 0.1$)

Fig. 7. Simulation study of grid-synchronizing stability (a balanced grid fault is applied 2s with a duration of 625 ms, $\alpha_{\text{pll}} = 50Hz$, $\bar{\boldsymbol{I}}_{\text{c}} = 1 + 0 \cdot \text{j}$, $\bar{\boldsymbol{Z}}_{\Sigma} = 0.2\text{j}$, $\bar{\boldsymbol{Z}}_{\text{s}} = 0.1\text{j}$)

Next, the phase portrait under a severe grid fault is presented in Fig. 7 (b) (i.e. $\boldsymbol{k}_{\text{f}} = 0.1$). According to the simulation configurations, trajectories of the phase portrait should follow the mechanism illustrated in Fig. 3 (a). Moreover, the EAP is not satisfied in this case, which means loss of synchronization is expected after the fault is cleared. This can be clearly identified in Fig. 7 (b), where the phase portraits diverge from the original equilibrium (point A in Fig. 3 (a)).

In Fig. 7 (c), time domain waveforms are given in accordance with the phase portrait in Fig. 7 (b). It is seen that the PLL frequency is driven away and a steady angle cannot be established after fault clearance indicating a loss of synchronization. Furthermore, it can also be found that the currents exhibit large transients due to the loss of synchronization. In practice, a full picture of these transients may not be seen due to the action of over-current/voltage protections. Consequently, this can easily be confused with the passive circuit transients if the mechanism behind GSS is not well-understood.

C. Simulation study of the estimated CCTs

In the following, the estimated CCT based on (9) will be compared with simulated results, and in this study, $k_{\text{c}} \approx 3/4$ is the default setting, another value $k_{\text{c}} \approx 1/2$ is also presented for the purpose of comparison. As the CCT is the maximum fault duration that is allowed while remaining synchronized after fault clearance. It is difficult to show the simulated results directly. The best way the authors come up with is to use the *time instant* at which the simulated angle reaches $\delta_{\text{pll}}^{\text{B}}$ (e.g. in Fig. 3 (a), it is an equilibrium in addition to $\delta_{\text{pll}}^{\text{A}}$, but here it is referred to as the critical angle) to compare with the analytical CCT. This is reasonable since $\left| f^{0-} \right| = \left| \bar{I}_{\text{cd}}^{\text{ref}} \bar{X}_{\Sigma} \right|$ is typically far smaller than $\left| g^{0-} \right| = \left| \boldsymbol{U}_{\text{pcc}}^{0\text{-}} \right|$ (e.g. if $\bar{I}_{\text{cd}}^{\text{ref}} = 1\,\text{pu}$ and $\bar{X}_{\Sigma} = 0.2$ pu, then $\left| f^{-} \right| = 0.2 \ll \left| g^{0-} \right| = 1$ since $\left| \boldsymbol{U}_{\text{pcc}}^{0\text{-}} \right| \approx 1$ pu), this means the CCA will be close to $\delta_{\text{pll}}^{\text{B}}$ according to EAP.

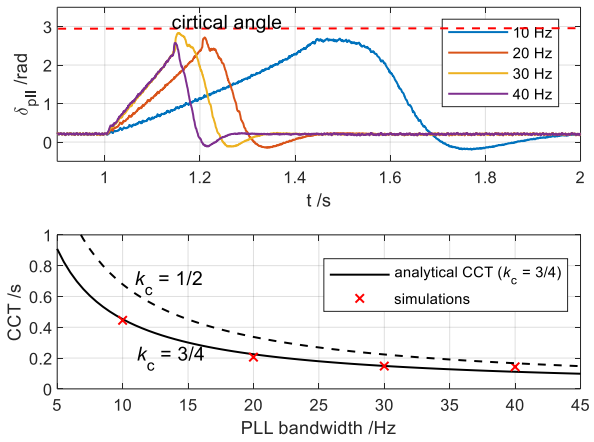

Fig. 8 Comparisons of the measured and analytical CCTs ($\bar{\boldsymbol{I}}_{\rm c} = 1 + 0 \cdot {\rm j}$ pu, $\bar{\boldsymbol{Z}}_{\Sigma} = 0.2{\rm j}$ pu, $\bar{\boldsymbol{Z}}_{s} = 0.1{\rm j}$ pu, $\boldsymbol{k}_{\rm f} = 0.2$, $\delta_{\rm pll}^{\rm B} \approx 3rad$)

Based on this strategy, the time instants at $\delta_{\rm pll}^{\rm B}$ (i.e. critical angle) are extracted from the upper plot of Fig. 8, and they are marked by *crosses* in the bottom plot of Fig. 8. It is seen that the analytical CCTs (at $k_{\rm c}$ = 3/4) are close to simulated results, particularly the trend of CCT with respect to the change of PLL bandwidth, thus the CCT is an effective tool for the GSS margin analysis. Nevertheless, some small discrepancies yet exist between the analytical CCTs (at $k_{\rm c}$ = 3/4) and the simulations, this may because of 1) $\delta_{\rm pll}^{\rm B}$ is an approximant of the CCA for easier illustration; 2) CCT is derived from the critical condition of EAP, where the damping of the system is ignored. Also, the numerical calculation of CCT itself is essentially an approximant, see the impacts of $k_{\rm c}$, where a linear approximation of $\Delta\omega_{\rm pll}$ (i.e. $k_{\rm c}$ = 1/2) is optimistic and is not as precise as the nonlinear one (i.e. $k_{\rm c}$ = 3/4). However, $k_{\rm c}$ is a parameter non-relevant to system dynamics, thus the choice of $k_{\rm c}$ does not change the stability trends, thus the knowledge of the GSS margin analysis is not affected.

D. Effects of the PCC voltage phase shifts and reactive current injections on GSS

Based on the mechanism analysis of Fig. 3. (b) it is already obtained that the phase shifts of PCC voltage (i.e. g^{0+}) may determine the direction of PLL frequency (i.e. $\omega_{\rm pll}$) motion under a less severe grid fault, where a new equilibrium may exist in the fault duration. In what follows, simulations with and without phase shift under a less severe grid fault condition (i.e. $\boldsymbol{k}_{\rm f} = 0.5\angle 0$ and $\boldsymbol{k}_{\rm f} = 0.5\angle -\frac{\pi}{4}$) are conducted and presented in Fig. 9 (a) (please note that the angle differences are measured in PLL frame i.e. $\delta_{\rm pll}^{sim} = \theta_{\rm pcc} - \theta_{\rm pll}$, hence this simulated angle is opposite to that of the analytical models, i.e. $\delta_{\rm pll} = -\delta_{\rm pll}^{sim}$).

It is seen that the PLL frequency response with a phase shift is in the opposite direction of the one without phase shift, indicating the phase shift indeed has impacts on the direction of PLL frequency motion during the transients. Specifically, one could easily verify that the PLL frequency response with a phase shift follows the mechanism of Fig. 3. (b), where at the fault instant (i.e. point A in Fig. 3. (b)), $\omega_{\rm pll}$ initially decreases due to the condition: $\left|g^{0+}\right| > \left|f^{0+}\right|$, then it converges to point D due to EAP is met.

If no phase shift is presented, as discussed below the Fig. 3. (b), the new equilibrium point D in the fault duration should locate at the right side of the original equilibrium point A. This indicates that, at the fault instant, the condition $\left|g^{0+}\right| < \left|f^{0+}\right|$ is met, hence the PLL frequency will initially increase then converge to point D while the EAP is met. It is easily verified that the simulation under the no phase shift condition also follows the above-mentioned mechanism. Therefore, this simulation study proves that the analysis regarding the phase shift effects is correct.

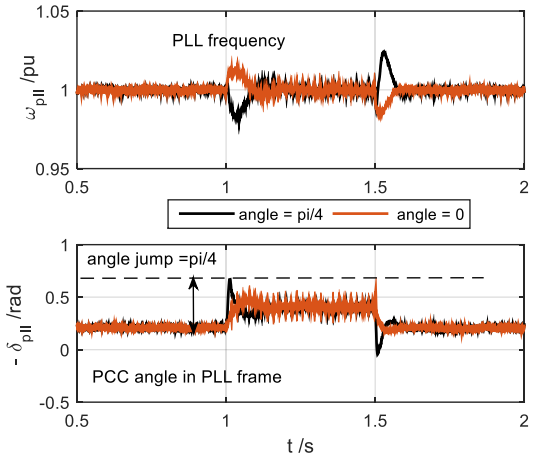

(a) Effects of PCC voltage phase shifts ($\bar{\boldsymbol{I}}_c = 1 + 0 \cdot \mathrm{j}$, $\bar{\boldsymbol{Z}}_\Sigma = 0.2\mathrm{j}$, $\bar{\boldsymbol{Z}}_s = 0.1\mathrm{j}$, $\alpha_{\mathrm{pll}} = 40Hz$, with phase shift i.e. $\boldsymbol{k}_f = 0.5\angle -\frac{\pi}{4}$, without phase shift $\boldsymbol{k}_f = 0.5\angle 0$)

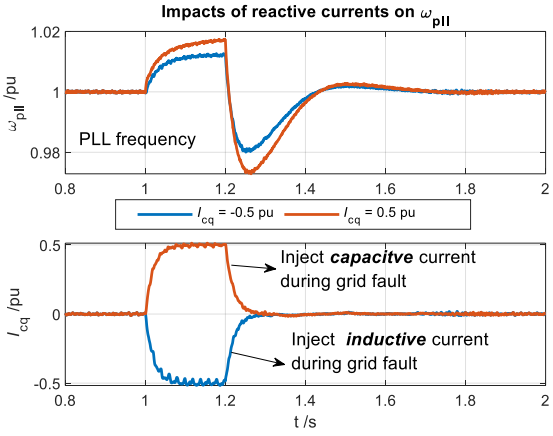

(b) Effects of reactive current injections ($\bar{I}_{cd}^{pll} = 1$, $\bar{\boldsymbol{Z}}_s = 0.1\mathrm{j}$, $\alpha_{\mathrm{pll}} = 10Hz$, $\boldsymbol{k}_f = 0.2\angle 0$, $\bar{\boldsymbol{Z}}_\Sigma = 0.23 + 0.19\mathrm{j}$ pu, X/R = 4)

Fig. 9 Simulation studies of the effects of PCC voltage phase shifts and reactive currents injections

In the next, the effects of reactive currents injections during grid faults on the GSS stability margin will be analyzed in terms of the time-domain response of PLL frequency. First, according to the acquired knowledge, the reactive current injection could take effects on the GSS only if the line resistance is nonzero. Therefore, in the simulation, the line impedance $\bar{\boldsymbol{Z}}_\Sigma$ with an X/R =4 is adopted, and a severe grid fault with no phase shift is considered, i.e. $\boldsymbol{k}_f = 0.2\angle 0$, the positive direction of the current is flowing into the grid, thus a negative value of I_{cq} denotes an inductive current injection whereas a positive value of I_{cq} denotes a capacitive current injection.

As shown in Fig. 9 (b), the deviation of the transient PLL frequency ω_{pll} is smaller when injecting an inductive current into the faulty grid than that of a capacitive one. This is because $f = \bar{I}_{cq}^{ref} \bar{R}_\Sigma + \bar{I}_{cd}^{ref} \bar{X}_\Sigma$ is smaller if $\bar{I}_{cq}^{ref} \approx \bar{I}_{cq}$ is negative, and this will result in a smaller acceleration area S_I according to the mechanism analysis of Fig. 3. (a), consequently a small deviation of ω_{pll} is

expected under such a condition. It should be noted again that the effects of reactive current injections on GSS could be marginal if the line resistance is negligible, this is mostly true for large-scale wind farms connected to high voltage transmission systems. If the resistance cannot be ignored, coordinated control of active and reactive current when fulfilling the LVRT should be carefully examined since their composite effect on f may result in different transient behavior of grid-synchronization [30].

VI. Conclusions

This paper explored and clarified the GSS issue that may have been overlooked in the conventional transient analysis of wind turbines or generally the grid-tied VSCs. The mechanism behind this GSS is revealed by a nonlinear model and the EAP, which is primarily caused by the transient interaction between the PLL and the faulty grid. A quantitative assessment of the GSS margin is performed by further calculating the CCT, where the impacts of the PLL bandwidth, the faulty voltage (magnitude and phase shift), as well as the reactive current injection are evaluated, and the main findings are summarized as follows:

1) PLL bandwidth has the most evident effects on the GSS compared to the other two factors, and a small PLL bandwidth can drastically increase the CCT, i.e. the GSS margin is improved.

2) For a less severe grid fault, usually, it is not a threat to the GSS since the system exists a stable equilibrium during the grid fault, however, the phase shift of the faulty voltage may result in different motion directions of the re-synchronization. For a severe grid fault, the effects of phase-shift are marginal due to the low-voltage while the GSS becomes the major concern. It turns out that the system can easily lose synchronization if the grid fault is not cleared in a fast way, i.e. within the CCT.

3) The reactive current injection can affect the GSS only if the resistive part of the line impedance (from the VSC terminal to PCC) is evident, thus it may not be a major concern for wind farms tied to high-voltage transmission systems. Otherwise, the impacts of the reactive current injection, particularly in fulfilling the LVRT scheme should be carefully examined according to the proposed GSS analysis.

In addition, parameter tuning of the PLL for the stability purpose can be easily fulfilled through the same method as the GSS margin assessment. For example, if the electrical system of a wind farm is determined and given, the feasible PLL bandwidth complying with the grid code can be obtained from the numerical plot as Fig.5 (a), e.g., for the LVRT standard of China, wind turbines should remain connected for at least 625 ms under a low-voltage condition at the PCC (0.2 p.u.), in this case, the predicted PLL bandwidth is around 7 Hz as shown in Fig.5 (a). It should be noted that this design is focused on the intrinsic property of the system, if effective stabilization control is proposed and employed, a faster PLL is thus achievable.

Overall, this paper provides a systematic analysis of the GSS issue that could exist in systems with the VSC as the grid-interface，and the obtained knowledge could be useful for other nonlinear phenomenon analysis with less or relaxed assumptions (e.g. the

MA1,2 and the damping issue of EAP). Therefore, for more precise analysis, improved methods are expected to be explored and developed in future works.

ACKNOWLEDGMENT

The work and related research are supported under the Grant National Natural Science Foundation of China (51837007), and the Grant Norwegian University of Science and Technology (NTNU) (NTNU Energy, 81617922).

APPENDIX

A. Proof of quasi-static CCL in PLL time frame

Dynamics of CCL with an ideal compensation of cross-coupling and grid voltage can be approximately modeled as a first-order system, hence the CCL model in combination with the PLL regulator model can be written as:

$$\begin{cases} T_{\mathrm{c}} \dfrac{d\boldsymbol{I}_{\mathrm{c}}^{\mathrm{pll}}}{dt} = \boldsymbol{I}_{\mathrm{c}}^{\mathrm{ref}} - \boldsymbol{I}_{\mathrm{c}}^{\mathrm{pll}} \\ T_{\mathrm{pll}} \dfrac{d\Delta\omega_{\mathrm{pll}}}{dt} = u_{\mathrm{pccq}}^{\mathrm{pll}} + \dfrac{k_{\mathrm{p}}^{\mathrm{pll}}}{k_{\mathrm{i}}^{\mathrm{pll}}} \dot{u}_{\mathrm{pccq}}^{\mathrm{pll}} \\ \dfrac{d\Delta\theta_{\mathrm{pll}}}{dt} = \Delta\omega_{\mathrm{pll}} \end{cases} \tag{A.1}$$

where, $u_{\mathrm{pccq}}^{\mathrm{pll}} = f\left(\boldsymbol{I}_{\mathrm{c}}^{\mathrm{pll}}, \Delta\omega_{\mathrm{pll}}, \ \Delta\theta_{\mathrm{pll}}\right)$. If dynamics in PLL time frame will be analyzed, a transformation for t can be used as $\tau = t / T_{\mathrm{pll}}$. Hence (A.1) can be rewritten as:

$$\begin{cases} \varepsilon \dfrac{d\boldsymbol{I}_{\mathrm{c}}^{\mathrm{pll}}}{dt} = \boldsymbol{I}_{\mathrm{c}}^{\mathrm{ref}} - \boldsymbol{I}_{\mathrm{c}}^{\mathrm{pll}} \\ \dfrac{d\Delta\omega_{\mathrm{pll}}}{d\tau} = u_{\mathrm{pccq}}^{\mathrm{pll}} + \dfrac{k_{\mathrm{p}}^{\mathrm{pll}}}{k_{\mathrm{i}}^{\mathrm{pll}}} \dot{u}_{\mathrm{pccq}}^{\mathrm{pll}} \end{cases} \tag{A.2}$$

where $\varepsilon = T_{\mathrm{c}} / T_{\mathrm{pll}}$. Due to CCL is much faster than PLL $\varepsilon \approx 0 \rightarrow \boldsymbol{I}_{\mathrm{c}}^{\mathrm{ref}} \approx \boldsymbol{I}_{\mathrm{c}}^{\mathrm{pll}}$ and $\hat{u}_{\mathrm{pccq}}^{\mathrm{pll}} \approx f\left(\boldsymbol{I}_{\mathrm{c}}^{\mathrm{ref}}, \Delta\omega_{\mathrm{pll}}, \ \Delta\theta_{\mathrm{pll}}\right)$, where $\hat{u}_{\mathrm{pccq}}^{\mathrm{pll}}$ is referred to as the *quasi-static* model in PLL time frame. Similar analysis can be applied to other circuit elements, e.g. voltage drop across the impedance is: $\Delta\hat{\boldsymbol{u}}_{\mathrm{line}} = \boldsymbol{I}_{\mathrm{c}}^{\mathrm{ref}}\left(R_{\mathrm{line}} + \mathrm{j}\omega_{\mathrm{pll}} L_{\mathrm{line}}\right)$. One may refer to [31] for more details regarding the modeling of a singular perturbed system, i.e. a system with multiple time scales.

REFERENCES

[1] R. Teodorescu, M. Liserre, and P. Rodriguez, “Introduction,” in Grid converters for photovoltaic and wind power systems, Chichester, United Kingdom: John Wiley & Sons, 2011, pp. 1–4.

[2] B.Wu, Y.Q. Lang, N. Zargari and S. Kouro, "Power Converters in Wind Energy Conversion Systems," in Power Conversion and Control of Wind Energy

Systems , Wiley-IEEE Press, 2011.

[3] H.K. Liu, X.R. Xie, J.B. He, T. Xu, Z. Yu, C. Wang and C.Y. Zhang. "Sub-synchronous Interaction Between Direct-Drive PMSG Based Wind Farms and Weak AC Networks," in IEEE Transactions on Power Systems, vol. 32, no. 6, pp. 4708-4720, Nov. 2017.

[4] C. Li, "Unstable Operation of Photovoltaic Inverter From Field Experiences," in IEEE Transactions on Power Delivery, vol. 33, no. 2, pp. 1013-1015, April 2018.

[5] B. Wen, D. Boroyevich, R. Burgos, P. Mattavelli and Z. Shen, "Analysis of D-Q Small-Signal Impedance of Grid-Tied Inverters," in IEEE Transactions on Power Electronics, vol. 31, no. 1, pp. 675-687, Jan. 2016.

[6] M. Cespedes and J. Sun, "Impedance Modeling and Analysis of Grid-Connected Voltage-Source Converters," in IEEE Transactions on Power Electronics, vol. 29, no. 3, pp. 1254-1261, March 2014.

[7] C. Zhang, X. Cai, A. Rygg and M. Molinas, "Sequence Domain SISO Equivalent Models of a Grid-Tied Voltage Source Converter System for Small-Signal Stability Analysis," in IEEE Transactions on Energy Conversion, vol. 33, no. 2, pp. 741-749, June 2018.

[8] A. Rygg, M. Molinas, C. Zhang and X. Cai, "A Modified Sequence-Domain Impedance Definition and Its Equivalence to the dq-Domain Impedance Definition for the Stability Analysis of AC Power Electronic Systems," in IEEE Journal of Emerging and Selected Topics in Power Electronics, vol. 4, no. 4, pp. 1383-1396, Dec. 2016.

[9] J. Sun, "Impedance-Based Stability Criterion for Grid-Connected Inverters," in IEEE Transactions on Power Electronics, vol. 26, no. 11, pp. 3075-3078, Nov. 2011.

[10] C. Zhang, X. Cai, Z. Li, A. Rygg and M. Molinas, "Properties and physical interpretation of the dynamic interactions between voltage source converters and grid: electrical oscillation and its stability control," in IET Power Electronics, vol. 10, no. 8, pp. 894-902, 6 30 2017.

[11] D. Dong, B. Wen, D. Boroyevich, P. Mattavelli and Y. Xue, "Analysis of Phase-Locked Loop Low-Frequency Stability in Three-Phase Grid-Connected Power Converters Considering Impedance Interactions," in IEEE Transactions on Industrial Electronics, vol. 62, no. 1, pp. 310-321, Jan. 2015.

[12] A.D. Hansen and G. Michalke. "Fault ride-through capability of DFIG wind turbines." Renewable Energy 32(9):1594-1610, 2007.

[13] J. Morren and S. W. H. de Haan, "Ridethrough of wind turbines with doubly-fed induction generator during a voltage dip," in IEEE Transactions on Energy Conversion, vol. 20, no. 2, pp. 435-441, June 2005.

[14] S. Xiao, G. Yang, H. Zhou and H. Geng, "An LVRT Control Strategy Based on Flux Linkage Tracking for DFIG-Based WECS," in IEEE Transactions on Industrial Electronics, vol. 60, no. 7, pp. 2820-2832, July 2013.

[15] S. Hu, X. Lin, Y. Kang and X. Zou, "An Improved Low-Voltage Ride-Through Control Strategy of Doubly Fed Induction Generator During Grid Faults," in IEEE Transactions on Power Electronics, vol. 26, no. 12, pp. 3653-3665, Dec. 2011.

[16] M. Rahimi and M. Parniani, "Coordinated Control Approaches for Low-Voltage Ride-Through Enhancement in Wind Turbines With Doubly Fed Induction Generators," in IEEE Transactions on Energy Conversion, vol. 25, no. 3, pp. 873-883, Sept. 2010.

[17] R. Ottersten, A. Petersson, and K. Pietiläinen, "Voltage Sag Response of PWM Rectifiers for Variable-Speed Wind Turbines," in Energy Engineering, vol.16, no. 1, pp.6-14, 2004.

[18] M. Singh and A. Chandra, "Power maximization and voltage sag/swell ride-through capability of PMSG based variable speed wind energy conversion system," 2008 34th Annual Conference of IEEE Industrial Electronics, Orlando, FL, pp. 2206-2211, 2008.

[19] S. Alepuz, A. Calle, S. Busquets Monge, S. Kouro and B. Wu, "Use of Stored Energy in PMSG Rotor Inertia for Low-Voltage Ride-Through in Back-to-Back NPC Converter-Based Wind Power Systems," in IEEE Transactions on Industrial Electronics, vol. 60, no. 5, pp. 1787-1796, May 2013.

[20] R. J. Nelson, H. Ma and N. M. Goldenbaum, "Fault ride-through capabilities of siemens full-converter wind turbines," 2011 IEEE Power and Energy Society General Meeting, San Diego, CA, pp. 1-5, 2011.

[21] J. Hu, Q. Hu, B. Wang, H. Tang and Y. Chi, "Small Signal Instability of PLL-Synchronized Type-4 Wind Turbines Connected to High-Impedance AC Grid

During LVRT," in IEEE Transactions on Energy Conversion, vol. 31, no. 4, pp. 1676-1687, Dec. 2016.

[22] J. Hu, B. Wang, W. Wang, H. Tang, Y. Chi and Q. Hu, "Small Signal Dynamics of DFIG-Based Wind Turbines During Riding Through Symmetrical Faults in Weak AC Grid," in IEEE Transactions on Energy Conversion, vol. 32, no. 2, pp. 720-730, June 2017.

[23] I. Erlich, F. Shewarega, S. Engelhardt, J. Kretschmann, J. Fortmann and F. Koch, "Effect of wind turbine output current during faults on grid voltage and the transient stability of wind parks," 2009 IEEE Power & Energy Society General Meeting, Calgary, AB, pp. 1-8, 2009.

[24] J. Martinez, P.C. Kjær, P. Rodriguez, and R. Teodorescu, "Active current control in wind power plants during grid faults," in Wind Energy, vol.13, no. 8, pp.737-749, 2015.

[25] Ö. Göksu, R. Teodorescu, C. L. Bak, F. Iov and P. C. Kjær, "Instability of Wind Turbine Converters During Current Injection to Low Voltage Grid Faults and PLL Frequency Based Stability Solution," in IEEE Transactions on Power Systems, vol. 29, no. 4, pp. 1683-1691, July 2014.

[26] C. Zhang, X. Cai, Z. Li. "Transient Stability Analysis of Wind Turbines with Full-scale Voltage Source Converter," in Proceedings of the CSEE, vol. 37, no. 14, pp. 4018-4026, 2017 (in Chinese).

[27] H. Geng, L. Liu and R. Li, "Synchronization and Reactive Current Support of PMSG-Based Wind Farm During Severe Grid Fault," in IEEE Transactions on Sustainable Energy, vol. 9, no. 4, pp. 1596-1604, Oct. 2018.

[28] S. Ma, H. Geng, L. Liu, G. Yang and B. C. Pal, "Grid-Synchronization Stability Improvement of Large Scale Wind Farm During Severe Grid Fault," in IEEE Transactions on Power Systems, vol. 33, no. 1, pp. 216-226, Jan. 2018.

[29] P. Kundur, J. Paserba, V. Ajjarapu, G. Andersson, A. Bose, C. Canizares, et al, "Definition and classification of power system stability IEEE/CIGRE joint task force on stability terms and definitions," in IEEE Transactions on Power Systems, vol. 19, no. 3, pp. 1387-1401, Aug. 2004.

[30] G. Han, C. Zhang, X.Cai, "Mechanism of frequency instability of full-scale wind turbines caused by grid short circuit fault and its control method," in Transactions of China Electrotechnical Society, vol.33, no.10, pp:2167-2175, May 2018 (in Chinese).

[31] Skinner, L. A. Singular perturbation theory. Springer Science & Business Media, 2011.